Multilayer resonant subwavelength gratings: effects of waveguide modes and real groove profiles

Leonid I. Goray

International Intellectual Group, Incorporated, P.O. Box 335, Penfield, New York 14526

Ivan G. Kuznetsov

Raytheon ITSS/NASA GSFC, Code 551, Greenbelt, Maryland 20771

Sergey Yu. Sadov

Department of Mathematics and Statistics, Memorial University of Newfoundland, St. John's, Newfoundland, Canada A1C 5S7

David A. Content

NASA GSFC, Code 551, Greenbelt, Maryland 20771

Received April 4, 2005; revised manuscript received August 4, 2005; accepted August 26, 2005

The boundary integral equation code PCGrate-S(X) is used to analyze diffraction on Hubble Space Telescope Cosmic Origins Spectrograph gratings at different boundary shapes and layer thicknesses. An effect of resonance anomalies excited in nonconformal dielectric layers overcoated on the surface of metallic grating on the efficiency is studied for the first time to our knowledge. Refractive indices (RIs) for bulk MgF_2 taken from well-known references are found to be not suitable for thin optical layers at wavelengths between 115 and 170 nm. A method based on scale fitting of calculated and measured grating efficiencies is outlined for derivation of thin-film optical constants at hard to measure wavelengths. The calculated efficiency based on real boundary profiles and derived RIs of the G185M subwavelength grating is shown to fit within 9.6% or better to the measured data. © 2006 Optical Society of America

OCIS codes: 050.1950, 050.1960, 260.2110, 260.7190, 310.2790, 310.6860.

1. INTRODUCTION

When the instruments were selected for the fifth (and last planned) servicing mission to the Hubble Space Telescope (HST), the Cosmic Origins Spectrograph (COS) was included as a much more sensitive UV spectrograph; the per-element performance increase burden fell chiefly on dispersive optics improvements. The design of the COS UV channel required highly dispersive optical elements capable of resolving the faintest point objects in a slitless spectrograph with at least 40% blaze efficiency.[1] The COS near-ultraviolet (NUV) channel (170–320 nm), divided into three separate wave bands, was covered by three high-dispersion and one low-dispersion gratings. The most challenging 5870 groove/mm G185M grating intended for operation at vacuum-UV (VUV) wavelengths below 200 nm has the highest groove density and the shortest operational wavelength range of all COS NUV gratings. The grating also turned out to be the most difficult to model. Initial modeling that exploited scalar theory failed completely; more-sophisticated modeling[2] made use of standard refractive-index (RI) libraries, and unscaled groove profiles data failed to reach even marginal agreement with experiment at wavelengths below 150 nm. At that time, for grating selection it was only natural to rely on the legacies of diffraction grating studies developed for the two most relevant grating-oriented projects: the Far Ultraviolet Spectroscopic Explorer (FUSE) and the Space Telescope Imaging Spectrograph (STIS). While FUSE had already successfully flown highly resolving 6000 groove/mm curved metal-coated gratings, the STIS grating program collected a wide database on development and testing of high-quality NUV flight gratings. Platinum ultrafine FUSE gratings coated with a SiC monolayer or an Al+LiF bilayer perform exceptionally well at wavelengths below 120 nm.[3,4]

The multilayer-coated COS NUV gratings were designed bearing in mind these successful experiences but with an application targeted at significantly longer wavelengths in order to provide assured long-term NUV spectroscopy for the Hubble Space Telescope. The efficiency measurements for coated gratings, however, were disastrous: none of the high-spectral-resolution NUV channel gratings met specifications after the final coating. It took long and exhaustive measurements and modeling efforts[2] to prove that the scalar approach is generally not applicable to multilayer-coated gratings. Resonance efficiency anomalies associated with waveguide funneling modes degrading the COS NUV grating performance were mea-

1084-7529/06/010155-11/$0.00 © 2006 Optical Society of America

sured and qualitatively described. The main unresolved modeling issue was the choice of RI data for efficiency modeling. Thorough modeling performed[2] for the COS NUV G185M grating by use of the optical constant data from Palik[5] produced only marginal agreement between theoretical and measured efficiency values at wavelengths in the 115–170 nm range, where a MgF_2 coating over Al is imperative to protect reflectance from degradation caused by oxidation. The reason for this modeling failure might arise from an RI data inconsistency in the far-ultraviolet FUV–NUV wave band. Most commonly used sources provide RI data for bulk materials. Recent studies carried out by Larruquert and Keski-Kuha[6] demonstrated, however, significant differences among the optical constants of ion-beam-sputtered, evaporated, and bulk MgF_2 at FUV wavelengths.

To model the efficiency of the G185M subwavelength grating we used the commercial program PCGrate,[7] which proved to be a reliable tool to study (at a reasonable computing cost) complex problems of diffraction on periodic gratings that require an accurate treatment of grating anomalies.[2,7–9] Reference 9 describes the modified integral method (MIM), which is a variant of the boundary integral equation method and is used to advantage in PCGrate-S(X) as applied to gratings having one boundary or two congruent (conformal case) or noncongruent (nonconformal case) boundaries. Section 2 of the present paper features the multiboundary integral solver of PCGrate-S(X), emphasizing details not found in the literature or specific to this implementation. Section 3 presents experimental results for COS NUV G185M gratings; more details on the experiment can be found in Ref. 2. Section 4 presents thorough efficiency modeling for a subwavelength grating with real [measured by atomic force microscopy (AFM)] boundary profiles and RIs taken from different sources, including best fits of calculated data to experimental ones. We solve indirectly the inverse problem of efficiency calculations to derive RIs in the vicinity of anomalies. One first finds a layer topographic distribution (boundary profiles and thicknesses) for a known RI distribution in a given spectral region; then for a known grating profile, one finds the unknown RI in another spectral range using scale fitting of calculated and measured grating efficiencies. Model-based exact computational efficiencies obtained with the PCGrate software[7] yield a better than 10% agreement (with respect to absolute values) with measured efficiencies at any wavelength in the 120–255 nm range. Conclusions are presented in Section 5.

2. MULTILAYER SOLVER OF PCGrate-S(X)

The multilayer integral solver is based on the algorithm first described in Ref. 10. A more transparent and detailed exposition, together with discussion of various marching schemes that avoid hypersingular potential operators, is given in Ref. 11. The scheme in our program is the original one of Maystre, that is, variant D in each layer by Pomp's classification (Ref. 11, p. 113).

Analytical aspects of boundary integral operators are well described in the literature; see, e.g., Ref. 11 and 12. Here we give some details of the PCGrate code, and particular algorithmic enhancements are described in Subsections 2.B and 2.C. In addition, the generalization of the energy conservation identity to multilayer gratings is presented in Appendix A.

A. Grating Geometry, Fields, and Potentials

Consider a multilayer structure (Fig. 1) consisting of $N+1$ homogeneous material layers $\Lambda_0, \ldots, \Lambda_N$, characterized by their RIs $\nu_j = (\epsilon_j \mu_j)^{1/2}$, $j=0, \ldots, N$, and N periodic interfaces $\tilde{\Gamma}_0, \ldots, \tilde{\Gamma}_{N-1}$. A fixed part of each interface $\tilde{\Gamma}_j$ embracing exactly one grating period will be denoted as Γ_j. [We prefer the enumeration beginning with 0 for two reasons. First, the material layer 0 is often air (or vacuum), so it is not in fact a part of a fabricated grating. Second, this enumeration is directly compatible with array indexing in C++, which is the language of choice for the software discussed.]

We refer to the semi-infinite layer Λ_0 as the top layer and to Λ_N as the bottom layer. It is assumed that the light is incident from Λ_0. The bottom layer is semi-infinite downward. We formally include it into consideration even if the lowest medium is a perfect conductor, in which case Λ_N is ignored in the computational procedure.

For every $j=0, \ldots, N-1$, the lower boundary of the layer Λ_j is $\tilde{\Gamma}_j$, which will be called the floor of layer Λ_j. Similarly, for each $j=0, \ldots, N-1$, we call the upper boundary $\tilde{\Gamma}_{j-1}$ of layer Λ_j the ceiling of Λ_j.

Note that we allow the y projections of the boundaries to be overlapping. This is vital in the modeling of coated gratings.

In this paper we are concerned with pure TE or TM polarizations and nonmagnetic media; therefore fields are represented by scalar functions. They would be two-component vector functions in the case of conical (off-plane) diffraction, which will be discussed in detail elsewhere. The total field in Λ_0 is the sum of the incident field $u_{\text{inc}}(x,y)$ and the reflected field $u_0(x,y)$. For $j \geqslant 1$, the induced field inside layer Λ_j is denoted as $u_j(x,y)$. The solver deals only with boundary values of the fields and their normal derivatives $v_j^{\pm}$. There are four values attributed to every boundary Γ_j: the upper values u_j^-, v_j^- (that belong to

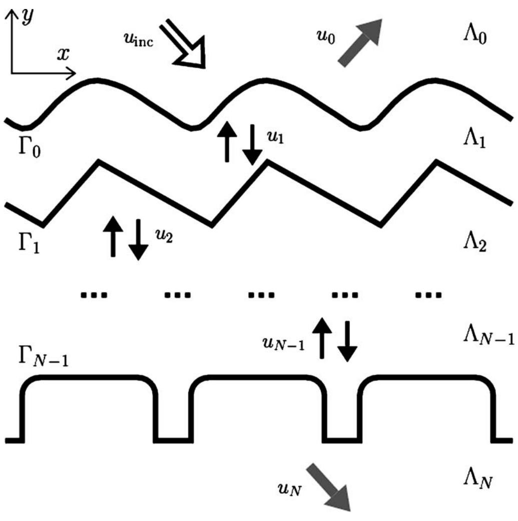

Fig. 1. Slab grating.

Table 1. Correspondence between Operator Notations in Two Papers

This Paper	Ref. 12
$\hat{S}_j$	G_+
$\check{S}_{j+1}$	G_-
$\hat{D}_j$	N_+
$\check{D}_{j+1}$	N_-

layer Λ_j and are the floor values for that layer) and the lower values u_j^+, v_j^+ (that belong to layer Λ_{j+1} and are the ceiling values for that layer).

Relations between boundary values of the fields across the layers can be found in terms of boundary potentials. Detailed discussion, formulas, and jump relations for potential operators can be found in many sources. Table 1 shows the correspondence between our notation and that in Ref. 11, p. 111. Our layers Λ_j, Λ_{j+1} correspond to Pomp's M_u, M_L, respectively.

The value of the field at any location can be found from the boundary data by a Green's formula. Inside the inner layer Λ_j, we have

$$u_j = \hat{S}_j[v_j^-] - \hat{D}_j[u_j^-] - \check{S}_j[v_j^+] + \check{D}_j[u_j^+]. \tag{1}$$

Evaluation of the potentials near boundaries involves singular integration and requires special numerical techniques (see, e.g., Ref. 13). Formulas for the diffracted field in Λ_0 and Λ_N contain only two terms. Diffraction efficiencies or far-field patterns for the reflected and transmitted fields can easily be found from the corresponding boundary values. Collecting the reflection and transmission coefficients, which are the summands in Eqs. (A3) and (A5), into vectors **r** and **t**, one can express them in a compact form as

$$\mathbf{r} = S_0^{+\infty}[v_0^-] - D_0^{+\infty}[u_0^-],$$

$$\mathbf{t} = D_N^{-\infty}[u_N^+] - S_N^{-\infty}[v_N^+], \tag{2}$$

with appropriate vector-valued functionals [Ref. 12, Eq. (26)] applied to the boundary functions. For lossy gratings, the absorption coefficients can also be calculated as a boundary integral from u_0^-, v_0^-, u_N^+, v_N^+ (see Appendix A).

As a potentially useful remark, let us note a certain freedom in the choice of the potential operators, more specifically of the Green functions (kernel functions). First, the kernels in the operators $\hat{S}_0$ and $\hat{D}_0$ in $\check{S}_N$ and $\check{D}_N$ must be outgoing upward and downward, respectively. This is dictated by the radiation conditions satisfied by the reflected and transmitted fields. It is not mathematically necessary that the Green functions in the inner layers possess such directional propagation properties, although it is customary to have downward propagating kernels in the $\check{S}_j$, $\check{D}_j$ $(j>0)$ operators and upward propagating kernels in the $\hat{S}_j$, $\hat{D}_j$ $(j<N)$ operators. Second, a Green function in an inner layer is defined up to the addition of an arbitrary solution of the homogeneous Helmholtz equation. In particular, an arbitrary finite linear combination of typical plane waves can be added to the Green function. To our knowledge, it seems that nobody has attempted to explore opportunities offered by this observation to improve the efficiency of Green function computations.

B. Discretization of Operator Equations

The choice of a numerical method to solve the boundary integral equations[11,12] is to a large extent independent of other implementation details of the algorithm. It is not even necessary to use the same method for every boundary provided that adjacent boundary solvers have a common data interface.

Our realization uses a rather simple but robust and universal method, the classical Nyström collocation.[14] The collocation points and the quadrature nodes can be interlacing or can be put at the same locations. The latter choice (our program's default option in most cases) requires a standard regularization of integrals.[12] It is worth noting that the regularization is used even at corner nodes of a nonsmooth boundary (see Ref. 11, p. 120). For relatively shallow profiles, the nodes can be uniformly put along the x coordinates. But the uniform distribution with respect to the arc length, as in Ref. 12, is more universal and makes it possible to treat, for example, lamellar or deep sinusoidal profiles by the integral method without any additional effort on the part of the user.

More details about the accuracy of the method and various options of the program can be found in Ref. 9 (Section 2.C). Convergence results can be proved rather painlessly if all the boundaries between the layers are smooth: One refers to standard properties of boundary potential operators in Sobolev spaces. Theoretically, in that case, a discrete sequence of frequencies may exist, for which the method will run into a noninvertible operator and the discretization will correspondingly run into an ill-conditioned matrix. The situation is more subtle if the boundaries have corners or cusps. It becomes much harder to prove solvability of operator equations and to investigate convergence of numerical methods. Mathematically, the dramatic gap between smooth and nonsmooth cases is due to different analytical properties of the potentials. For example, in the nonsmooth case the single-layer potential is no longer a compact operator in $L_2(\Gamma)$.[15] Theoretic estimations and explicit convergence exponents in the transmission problem with nonsmooth boundary and various discretization schemes have been worked out,[15–18] but to our knowledge there are no mathematical derivations of numerical convergence rates for multilayer structures.

Our experience with the current solver shows that discrete eigenvalues do not cause any real trouble and can be bypassed with a tiny deviation of parameters unless the number of layers becomes very big or a very thin layer is present. Convergence deteriorates at the presence of thin layers, at high frequencies, and at a large number of layers. For discussion of some crash test calculations on this code, we refer the reader to Ref. 9.

In spite of many research efforts (see, e.g., Ref. 19), computation of the kernels remains a time-critical part of the integral method for periodic structures. To accelerate convergence of the series representing the kernels, we use Aitken's δ^2 method, which is a simple one-term improvement over a popular acceleration (described, e.g., in Ref. 20, Section 3.8.2). More accurate Kummer and Euler–

Knopp acceleration techniques (see references in Ref. 9) make sense in combination with higher-order collocation or Galerkin methods. However, it is a difficult task to achieve an acceptable combination of robustness and wide-range applicability with higher-order codes.

C. Code Optimization

To reduce computing time for matrices of the discretized operator equations, two enhancements at the algorithmic level are used: cache for the Green functions and cache for exponential functions (plane waves). We describe these methods in order. Both assume a time–memory trade-off. The amount of memory required for cache can be calculated in advance in each case and adjustments (cache off or partial) are done automatically.

1. Cache for the Green Functions

Matrix entries of discretized integral equations are kernels of one of the three types: single-layer potential, its normal derivative, and double-layer potential. Any of these Green functions for the given layer has two vector arguments: the source position $\mathbf{x}$ and the observation point $\mathbf{x}_0$. The value of the Green function depends on the difference vector $\mathbf{d}=\mathbf{x}-\mathbf{x}_0$.

There are a number of cases of practical interest when the same difference vector $\mathbf{d}$ corresponds to more than one pair $\{\mathbf{x},\mathbf{x}_0\}$. Typical situations include the following:

(1) conformal layers: upper and lower boundaries of such a layer are obtained from each other by a vertical shift;

(2) more generally, layers whose boundaries are congruent by a translation (not necessarily in the vertical direction); and

(3) rectilinear segments of boundaries, if collocation points are uniformly distributed along such a segment.

In all these situations, it is possible to reuse values of the Green functions calculated earlier. The program stores the following data: type of potential and difference of arguments vector $\{\Delta\mathbf{x},\Delta\mathbf{y}\}$ in lexicographical order. Fast search and insertion are provided by a binary tree structure (Ref. 21, Section 4.4). Memory expenditure for the Green function cache is of the order of $CN_{\max}^2$ per layer, where $N_{\max}$ is the maximum number of collocation points on the boundaries, and the constant C incorporates the size of the data structure corresponding to each node of the tree. If no further layer has a RI of the current layer, then the cache gets overwritten as the solver proceeds to a new layer. However, it is quite typical to have a multilayer structure with repeating indices, in which case the Green functions computed for one layer have a chance to be reused in another layer. Note that the more effective the cache, the lesser the constant C (that is, the more that repetitions occur). To save memory without compromising accuracy to any noticeable extent, single precision values are used for the difference components $\Delta\mathbf{x},\Delta\mathbf{y}$.

2. Cache for Exponential Functions (Plane Waves)

Calculation of the Green functions makes extensive use of typical multiplicative combinations of exponential functions:

$$\exp\{i\alpha_m(x_j-x_n)+i\beta_m|y_j-y_n|\}=\begin{cases}E^+_{m,j}/E^+_{m,n} & \text{if } y_j\geqslant y_n;\\ E^-_{m,j}/E^-_{m,n} & \text{if } y_j<y_n.\end{cases} \tag{3}$$

Here

$$E^{\pm}_{m,j}=\exp(i\alpha_m x_j\pm i\beta_m y_j), \tag{4}$$

and α_m,β_m are defined in Eq. (A1). Let $\tilde{N}$ be the number of collocation points on a given boundary, that is, the subscripts j and n in the above expressions assume $\tilde{N}$ different values. Let P be the number of exponential terms to be stored in the cache. That is, the index m assumes P values situated symmetrically (with a possible ±1 imbalance) with respect to 0. Normally P is the maximum number of exponential terms used in computations of the Green functions. If, however, there is not enough fast memory in the system, a partial cache is used, where some exponents are precomputed and extracted from the cache in the course of Green function computations, while other exponents are evaluated on the spot.

In total, $2P\tilde{N}$ exponents are precomputed for every boundary. The value of P may vary depending on which (if at all) acceleration method is used for series summation for a Green function, but in most practical cases $P\leqslant\tilde{N}$. So memory expenditure is again of the order of $\tilde{N}^2$ per layer. The precomputed exponents share the same memory for every layer, so newer values override old ones. Unlike with Green function cache, saving the precomputed exponents for a potential reuse in further layers with the same RIs does not make much sense: Precomputation needs only $O(\tilde{N}^2)$ operations per layer, which is a tiny fraction of the total, which is of order of $\tilde{N}^3$.

Keeping track of the stored elements order in this case does not call for any special technique like binary trees: A two-dimensional array is all one needs. However, a difficulty of another sort pops up. The numbers β_m have nonzero imaginary parts when $|m|$ exceeds some m_0, and the asymptotic of $\mathrm{Im}(\beta_m)$ is linear as $|m|$ grows indefinitely. While the absolute values of the quotients in Eq. (3) never exceed 1, the numerators and denominators by themselves can easily go beyond the underflow or overflow limits [depending on the signs of y_j in Eq. (4)] in the standard floating-point arithmetic. For example, the values $\mathrm{Im}(\beta_m)=1000$ and $y_j=10$, though rather extremal, can occur in grating calculations, implying the values $E(m,j)\sim\exp(\pm 10^4)$.

To resolve this problem, the data $\{E_{m,j}\}$ are stored in the format {mantissa, exponent} (see Ref. 22, Section 4.B). We fix a huge positive B (the base); in the program $B=10^{20}$, a more or less arbitrary value. Every nonzero real or complex number X can be uniquely written in the form

$$X=B^qM, \qquad 1\leqslant|M|<B. \tag{5}$$

The number M (represented in the usual floating-point arithmetic) is the mantissa and the integer q is the power exponent of the base B. The 2 byte C type `short int` is used for q in the program, which suffices for all practical purposes.

The only arithmetical operation required for Eq. (3) is the division X/Y given that $|X| \leqslant |Y|$. Writing Y in the form similar to Eqs. (5), $Y = B^{q'}M'$, we obtain

$$\frac{X}{Y} = \begin{cases} M/M' & \text{if } q = q' \\ (M/M')B^{-1} & \text{if } q = q' - 1 \\ 0 & \text{if } q < q' - 1 \end{cases}. \tag{6}$$

The divisions on the right are carried out in the standard floating-point format.

3. EXPERIMENTAL DATA OVERVIEW

The COS NUV grating efficiency and scatter testing procedures and results obtained were described in considerable detail in Ref. 2. Almost 20 candidate flight gratings intended for four COS NUV subchannels were tested for absolute efficiency in various geometries. All measurements were performed using a Fully Automated Ultraviolet Scatter Tester[23] (FAUST) setup configured for the vacuum environment.[2]

Here we will focus on the performance of only one most interesting G185M grating intended for operation at the VUV wavelength band (under 200 nm) in –1st order at 34.7 deg incidence for nonpolarized (NP) light (polarization state of the test beam was measured to an uncertainty of ±2% at VUV wavelengths).

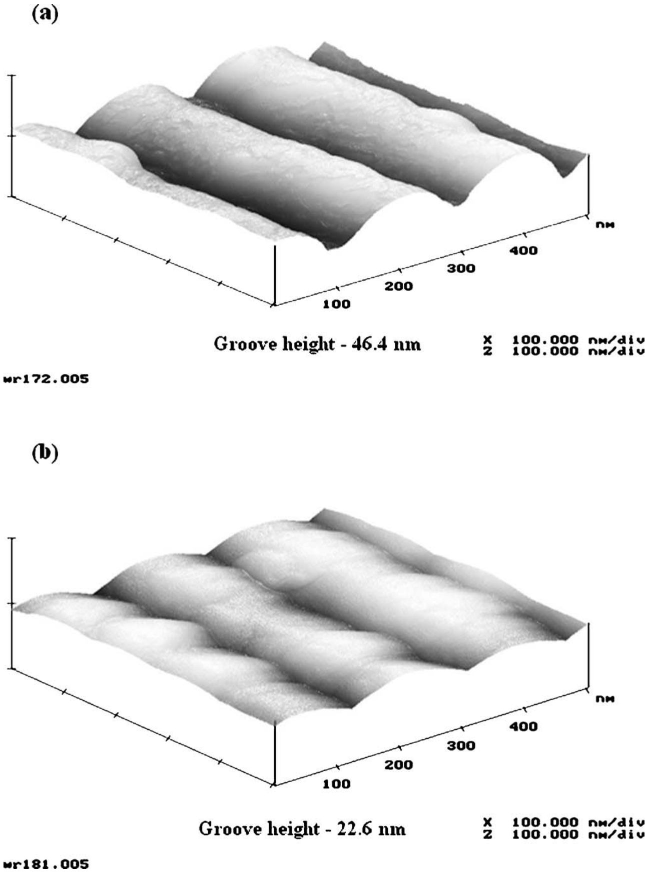

Fig. 2. AFM profilometry on a G185M grating performed by SPN Digital Nanoscope IIIA (a) before and (b) after Cr/Al/MgF_2 coating. Vertical scale is the same in both graphs.

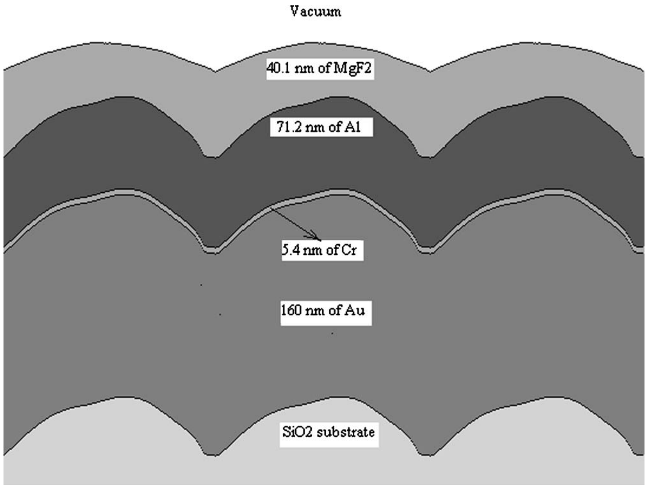

Fig. 3. Five-boundary G185M grating model. Horizontal and vertical scales are different.

At the time of performance characterization of the COS NUV gratings, the prime goal was to deliver optics satisfying the project minimum efficiency specification, and some interesting research-type tests were omitted to avoid the risk of damaging the flight hardware. For example, AFM grating surface profile measurements were performed on only one of the G185M Pt-coated master gratings and on only one of the fully coated Au/Cr/Al/MgF_2 G185M replica gratings.

The profile of the G185M grating (replica C) intended for operation in the 170–200 nm range was AFM measured before and after deposition of the Cr/Al/MgF_2 coating (Fig. 2). As seen from Fig. 2, after the deposition the profile depth decreased by approximately a factor of 2.05 (46.4 nm versus 22.6 nm), and the profile shape changed noticeably too, thus evidencing the case of nonconformal layering of the grating. For the reason that all G185M gratings were manufactured from the same master and by the same technology, one may suggest that all of them share before- and after-coating profiles. The layers deposited on the SiO_2 substrate are 160 nm Au, 5.4 nm Cr, 71.2 nm Al, and 40.1 nm MgF_2 (Fig. 3).

4. MODELING THE G185M GRATING

Initially, in this section the grating boundary profile is determined from the modeling at the wavelength range where the RI is reliable. Then the PCGrate-S(X) code is used to determine the grating efficiency as a function of the imaginary and real parts of the layer RI at the same incidence angles and wavelengths as those used in the experiment. Finally, the RIs of interest are derived by the least-squares fitting of modeling to experimental data. That reciprocal approach of retrieval of the RIs is fully feasible under two conditions: (1) when an exact method based on accurate vector theories is used and (2) when the precise layer boundaries are measured or calculated.[8,24] Such an indirect line of attack played a decisive role in our attempts to reach a good agreement between experiment and theory in the short-wavelength region, as discussed in Subsection 4.C.

Because of a small depth of light penetration into the metal, only two upper layers (Fig. 3) are essential for efficiency modeling. As this study has shown, the discrepancy between the calculated efficiencies in the two-boundary grating model with a semi-infinite Al layer and in the complete five-boundary model does not exceed a few hundredths of a percent throughout the wave band. This justifies our using the two-boundary model for efficiency modeling. The computational time, which is proportional to the number of layers at uncompromised accuracy, is thus reduced by a factor of ~2.5.

A. Influence of Layer Shapes on Efficiency

We start off by setting up a grating model for determination of the MgF_2–Al boundary profile, which is the least accurately known parameter. To determine which of the two AFM-measured boundary profiles, MgF_2 (border 1) or (Cr)–Au (border 2), is closer to the MgF_2–Al boundary, we started with modeling the NP efficiency of a two-boundary grating. We assume a conformal MgF_2 layer (the lower Al boundary is identical in shape to the MgF_2 one) with the 40.1 nm thickness. The calculated efficiencies (Fig. 4, double-dotted–dashed curve) differ from the measured values in time throughout the whole wavelength range, thus implying[2] invalidity of model 0 with a conformal layer. All calculated efficiency data presented in Subsection 4.A were obtained with the RIs of Al and MgF_2 taken from the handbook of Palik.[5] Although hereinafter the experimental efficiency data of two grating replicas (A and B) are displayed, we will focus primarily on discussing the grating A data (solid squares in Figs. 4, 7, and 9), because replica A is the grating on which more measurements were performed.

The next step is to use two models with nonconformal layers, one with the lower boundary being the same as the (Cr)–Au one (Fig. 4, short-dashed curve) and the other with the boundary scaled from (Cr)–Au at all points by a factor of 0.488 to the profile depth of the MgF_2 boundary (Fig. 4, dotted–dashed curve). In both cases, a vertical displacement of one boundary with respect to the other (shift of the boundary reference levels) was 40.1 nm, as in the conformal model. As evident from Fig. 4, the nonconformal model with unscaled lower boundary yields a noticeably superior qualitative agreement with experimental data. This suggests that the MgF_2–Al boundary more closely resembles the (Cr)–Au profile than the MgF_2 profile. The model takes into account the fact that the thickness difference of 23.8 nm between the lower and upper boundaries should be added to the conformal vertical displacement (40.1 nm) to obtain an adequate vertical displacement for the nonconformal MgF_2 layer. In this way the period-averaged thickness of the nonconformal MgF_2 layer is kept approximately equal to 40.1 nm within the boundary shape distortion.

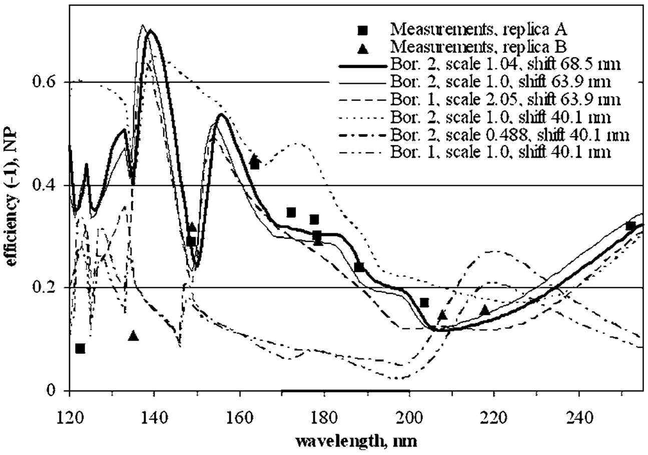

Fig. 4. Measured (points) and calculated (curves) –1st-order efficiency of a G185M grating for nonpolarization plotted versus wavelength. Efficiency models calculated for Palik's RIs and different geometry of a nonconformal MgF_2 layer: border (Bor.), scaling factor (scale), vertical shift (shift). A heavier region of the horizontal axis indicates the G185M intended operational range.

To determine the effect of profile shape, we set up models with equal depths and vertical shifts. The first one has the lower MgF_2 boundary scaled down to the (Cr)–Au boundary depth (making it smaller by a factor of 2.05) and a vertical displacement between the zero boundary levels equal to 63.9 nm. As seen from Fig. 4, the efficiency of this model (long-dashed curve) is close to that of another model with the unscaled (Cr)–Au lower boundary and a vertical shift of 63.9 nm (thin solid curve), while it is inferior by 40% or more as far as matching the experimental efficiencies. The latter suggests that, to set up an exact model, one has not only to determine the depth of the MgF_2–Al boundary but also to take into account the shape of its profile.

Having determined the type of the MgF_2–Al boundary profile, we have to refine it by scaling the shape in depth and then comparing the efficiencies obtained for each model with experimental data. Another fitting parameter is the vertical displacement of the boundaries. By automatic modeling of the efficiency over a small-meshed grid of these two parameters and wavelength, one can determine the average thickness of the MgF_2 layer from the best fit between the calculated and the experimental efficiencies. Even slight changes (with a few nanometers) in profile depth and vertical displacement give a noticeable rise to the efficiency at fixed wavelengths, particularly in resonance regions. Figure 4 presents an efficiency curve (bold solid curve) for model 1 with a lower-boundary scaling factor of 1.04 and a vertical displacement of 68.5 nm. The model with these parameters of the layer geometry provides the better least-squares fit (not worse than 19.8%) of calculated efficiency to experimental data, both in the medium and in the long-wavelength ranges. As to the short-wavelength part, no variations in the lower-boundary profile chosen within our approach yield theoretical values of the efficiency close enough to the measured ones.

B. Polarization Properties and Waveguide Modes

It is well known that a dielectric coating applied over a metallic grating brings about, other conditions being equal, the appearance of resonance anomalies associated with energy transport by leaky waveguide modes forming inside the dielectric.[25] The position and strength of these anomalies is intimately connected with trajectories of the scattering matrix poles and zeros of diffraction amplitudes in the complex plane, which are different for different polarizations (e.g., Ref. 20, Sections 5.3.2 and 5.4.1).

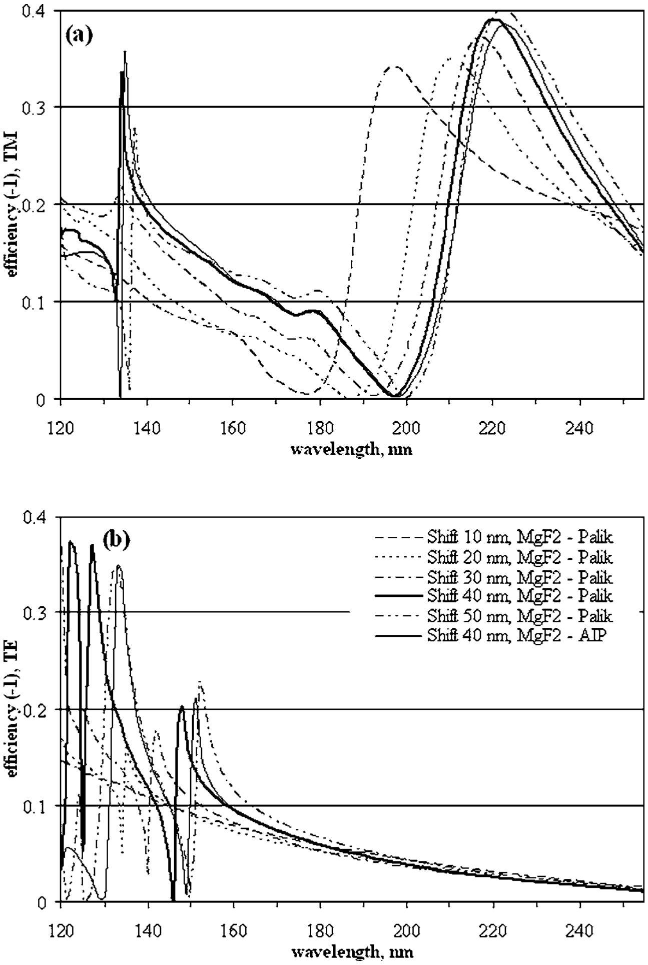

Fig. 5. Modeling of –1st-order efficiency of a G185M grating with a MgF_2 conformal layer for different RIs and thicknesses versus wavelength.[5,26] Thickness variations define the formation and positions of resonance anomalies: (a) TM polarization, (b) TE polarization. AIP, American Institute of Physics.

The phenomenological theory (polology) gives an insight into the origin and evolution of anomalies relating them to just a few parameters (poles, zeros).[25] In principle, polological calculations can be carried out using an integral method-based code provided that it is able to treat the incident wave vector with complex components. However, such formalism is more mathematically involved than our approach based on direct calculations of grating efficiency. The modeling presented in this subsection is connected only with the location and shape of the resonance anomalies in the efficiency curves. Essentially we adjust the parameters of the model step by step using a precise numerical tool to match resonances and to minimize discrepancies between measured and calculated efficiencies.

We start investigation of the formation of waveguide modes in real grating layers and their effect on the spectral efficiency curves with the conformal layer model similar to model 0 from Subsection 4.A. MgF_2 layer thickness variation shifts the efficiency of the resonance peaks significantly, as illustrated in Figs. 5(a) and 5(b). Here we use an unscaled MgF_2 AFM profile and RIs of both materials taken from Ref. 5. Figure 5(a) shows that the TM polarization threshold anomaly near 133.5 nm associated with the disappearance of the–2nd order becomes increasingly evident, while layer thickness (that is, vertical displacement for conformal layers) grows. At the MgF_2 layer thickness of 40 nm, this threshold anomaly is clearly pronounced, while at the thickness of 50 nm it transforms to a resonance anomaly near 136 nm.

The pattern is completely different for the TE polarization. At the 10 nm MgF_2 layer thickness, no anomalies are observed at all. At the layer thickness of 20 nm, a clearly seen resonance anomaly appears at 134 nm close to the threshold. While the waveguide layer thickness increases, the anomaly shifts to longer wavelengths and growth in amplitude. At the layer thickness of 50 nm, the efficiency drops to zero near the 150 nm wavelength. The increase in thickness also entails formation of other waveguide modes in the wavelength range down to ~133.5 nm, where a substantial number of diffraction orders propagate. At the layer thickness of 40 nm, those anomalies bear a distinct resonance pattern with narrow efficiency peaks with amplitude value differences of as much as 30% of absolute values.

Figures 5(a) and 5(b) also present efficiency curves calculated for the model with a 40 nm thick MgF_2 layer (thin solid curves) and RIs taken from Ref. 26. The difference of 5–10% in magnitude of the real parts of MgF_2 RIs taken from Ref. 26 in the region of anomalies compared with the data from Ref. 5 strongly affects the TE and TM efficiencies, noticeably shifting both the position and the amplitude of the anomalies. This effect is particularly clearly observed for the efficiency of the TE plane of polarization.

To study the anomalies in the grating model with a nonconformal layer, which is similar to model 1 from Subsection 4.A, let us calculate efficiencies with different scaling factors for the lower boundary, vertical displacements, and MgF_2 RIs. Figure 6 plots the modeled grating TE efficiency with the lower-boundary scaling factors of 0.9 and 1.1. As the vertical displacement and, accordingly, the average layer thickness increase, the edge of the anomaly shifts to longer wavelengths and its amplitude grows strongly, as is in the case of the conformal model. New anomalies appear in the short-wavelength domain. The amplitudes of the anomalies are appreciably larger

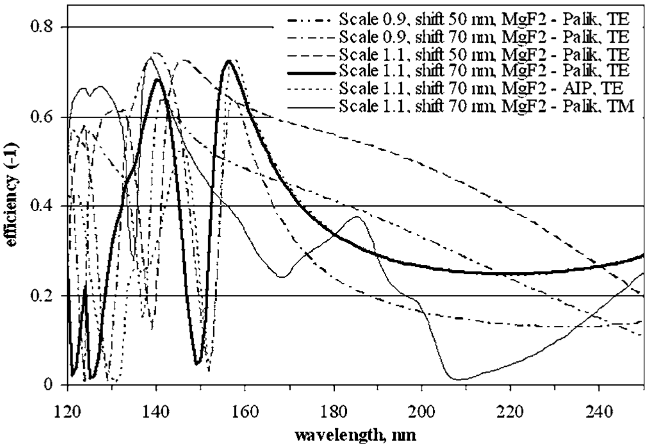

Fig. 6. Modeling of –1st-order efficiency of a G185M grating with a nonconformal MgF_2 layer for different RIs and geometry versus wavelength.[5,26] AIP, American Institute of Physics.

(up to 70% of absolute efficiency) than in the conformal case, which should be assigned to the larger depth of the lower boundary. In addition, unlike for the conformal model, the grating efficiency near anomalies is barely above zero, which can be attributed to the MgF_2 layer being nonconformal. Note that an increase in depth of the second boundary and, consequently, the degree of nonconformality of the layer makes the shape of the anomalies more complex as compared with the conformal case.

Figure 6 also presents the calculated efficiency for the same model but with a lower-boundary scaling factor of 1.1, vertical-boundary displacement of 70 nm, and RIs of MgF_2 taken from Ref. 26. As in the case of the conformal layer model, the positions, amplitudes, and the appearance of the anomalies vary considerably with the slightest changes in the RI. Also, the difference in the behavior of the efficiencies is more clearly observed (bold solid and shot-dashed curves, respectively) for the curves calculated for the RI taken from Ref. 26 rather than from Ref. 5. Although the TE efficiency curve approaches values close to zero at short wavelengths due to the anomaly and the TM efficiency curve (Fig. 6, thin solid curve) for the lower-boundary scaling factor of 1.1, displacement of 70 nm, and MgF_2 RI taken from Ref. 6 also exhibits resonance behavior, the average unpolarized light efficiency exceeds the absolute value of 30% under that model. The magnitudes and positions of the resonance anomalies, bad as they are, are playing a decisive role in the behavior of TE efficiency in the near Lyman-α and mid-VUV wavelengths and must account for the extremely low experimentally observed efficiencies at shorter wavelengths (Fig. 6).

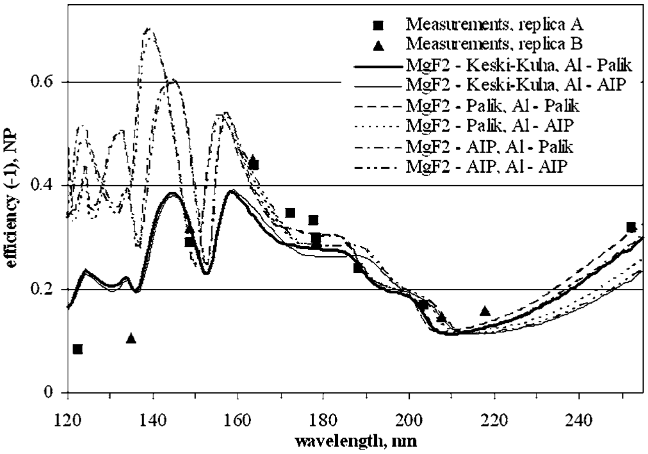

Fig. 7. Measured (points) and calculated (curves) –1st-order efficiency of a G185M grating for nonpolarization plotted versus wavelength.[5,26,27] Efficiency models calculated for the nonconformal MgF_2 layer (border 2, scale of 1.04, shift of 68.5 nm) and RIs of Al and MgF_2 are taken from different sources. AIP, American Institute of Physics.

C. Deriving Factual MgF_2 Refractive Indices from Efficiency Modeling

The efficiency curves calculated for model 1 for various combinations of the RIs of the materials taken from Refs. 5, 26, and 27 are presented in Fig. 7. A twofold better fit to measured efficiencies in the short-wavelength range is reached for the MgF_2 RI taken from Ref. 27 rather then from Refs. 5 and 26. The radical improvement is due to the noticeable absorption evident at wavelengths beyond 112 nm for the MgF_2 RI taken from Ref. 27. Figure 8 illustrates the difference trend of imaginary parts of the MgF_2 RI taken from different sources. Still, despite the considerably better agreement between theoretical and experimental data at the short-wavelength region, the absorption coefficients taken from Ref. 27 are smaller near the absorption edge for the model to produce a real quantitative fit. The curve at Fig. 7 (bold solid curve) with the Al RI taken from Palik's handbook demonstrates a good quantitative agreement with experiment at all points in the medium- and long-wavelength parts of the range, with the exclusion of points near 163 nm. The behavior of

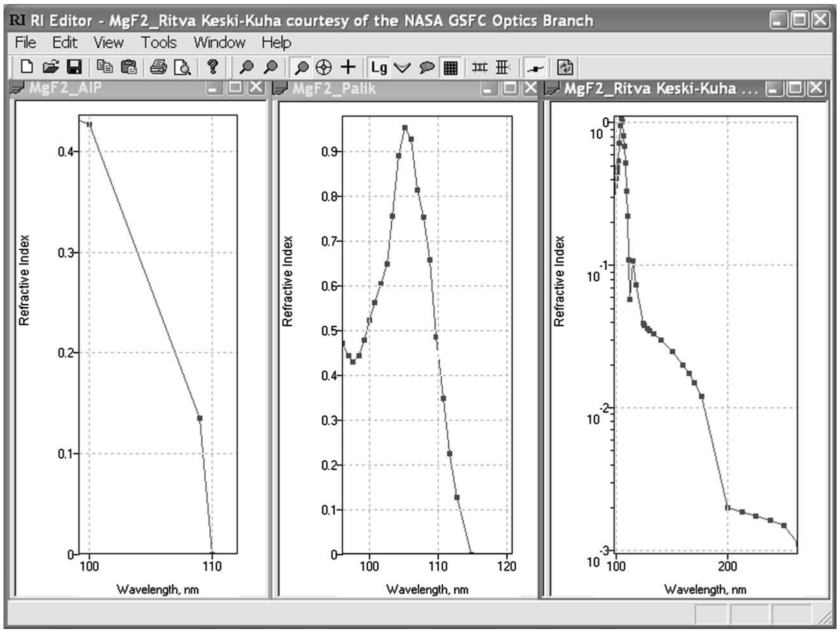

Fig. 8. Imaginary part of MgF_2 RIs in the FUV taken from different sources.

this theoretical curve over the 160–180-nm interval and the comparison of the calculated and measured data suggest an overestimation of absorption in this region from use of the MgF_2 RI taken from Ref. 27. On the whole, however, model 2 with the RI of MgF_2 from Ref. 27 and of Al from Ref. 5 provide a qualitatively correct fit to the behavior of efficiency throughout the wavelength range from 120 to 255 nm.

The result described above stimulates further refinement of the model now aimed at obtaining a correct RI of MgF_2. A comparison of the exactly calculated grating efficiency with measured values offers a possibility to not only find discrepancies between the tabulated and factual values of optical constants, but also to solve the inverse problem, i.e., to derive the RI of a layer material from the grating efficiency data.[28,29] The idea that underlies the proposed method is based on the nonscalar properties of the grating efficiency inherent in certain modes of its operation. Given other fixed parameters, the efficiency behavior of a grating cannot be described by the scalar theory of diffraction unless the ratio between relative and absolute grating efficiencies is proportional to the coating agent reflectance. We will illustrate the point by the following example explaining the grating efficiency modeling as an instrument used to extract the RI of MgF_2 from the measured grating efficiencies data.

In setting up the last grating model, we shall start from the layer's geometry of model 1 developed in Subsection 4.A. As was done with the models 1 and 2, we use the Al RI from Ref. 5. In view of the fact that the RI of MgF_2 from Ref. 27 provided a better fit to the measured efficiencies in model 2 throughout the wavelength range covered, we kept the real part of the MgF_2 RI from Ref. 27 in the new grating model unchanged. We shall be searching for the unknown imaginary part of the RI in the form of a piecewise linear function with nodes through every 10 nm, starting from 120 nm. Considering that the absorption at the MgF_2 layer beyond 170 nm (as is evident from a comparison of calculations with experiment) is small, we will set the imaginary part of the MgF_2 RI, starting from 170 nm and further into the long-wavelength region, to zero. We now have to determine the slopes of the piecewise linear function over the 120–170 nm interval. Since only three experimental points were measured for grating A in this range, we shall improve the accuracy by adding an other data point, measured on grating B at 134.8 nm. Next we perform least-squares fitting of the calculated efficiency curve for those four points with a step of 0.01 for the imaginary part of the RI. The values of the imaginary part of the RI for MgF_2 obtained this way are listed in Table 2. To smooth out the function we then replaced the derived modeling zero value of the imaginary part of the RI of MgF_2 at 160 nm with the 0.001 value; such a small fit practically does not change the efficiency value at that wavelength. We shall call the grating model with the RI of MgF_2 from Table 2 model 3.

Table 2. MgF_2 RIs for Evaporated Thin Films with Layer Thicknesses ~40 nm Derived from Efficiency Modeling

λ (nm)	Re(RI)	Im(RI)
120	1.759	0.12
130	1.653	0.1
140	1.603	0.06
150	1.554	0.04
160	1.482	0.001
170	1.468	0
180	1.451	0
190	1.442	0
200	1.439	0
212.5	1.437	0
225	1.434	0
237.5	1.432	0
250	1.43	0
262.5	1.4275	0

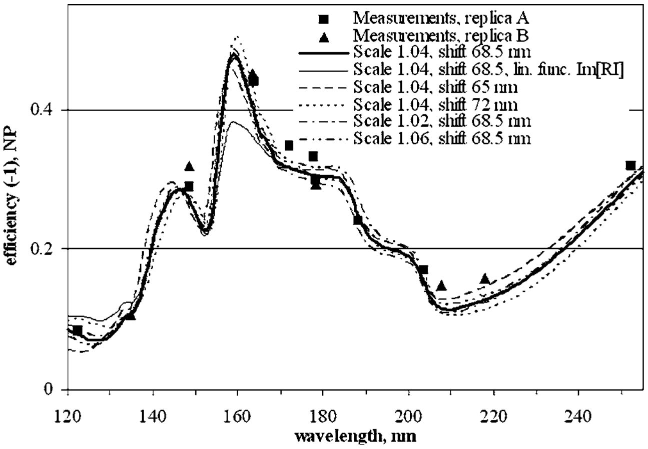

Fig. 9. Measured (points) and calculated (curves) –1st-order efficiency of a G185M grating for nonpolarization plotted versus wavelength. Efficiency models calculated for accurately derived and linearly scaled (lin. func. of Im[RI]) RIs and different geometry of a nonconformal MgF_2 layer.

Figure 9 plots the efficiency curve obtained for model 3 RIs (bold solid curve). What only remains is to check whether the average-thickness parameters of the MgF_2 nonconformal layer used in model 3 provide a better fit between the calculated and experimental values of efficiency throughout the wavelength range with a new RI library. To do this, we scale the vertical displacement and boundary parameters for model 3. Graphical results of this three-parameter optimization (scale, shift, and wavelength) are displayed in Fig. 9. An analysis of these results shows that the parameters of model 3 do indeed provide the best agreement between the measured and calculated values of efficiency throughout the wavelength range. The relative deviation of experiment from theory for all wavelengths at which grating A was studied does not exceed 9.6% throughout the wavelength range. Finally, we will demonstrate the outcome of the imaginary part of the MgF_2 RI changes on the G185M grating efficiency. To do that we compile a library similar to the one used in model 3 but with the imaginary parts of the RIs decreasing linearly from 0.1 to 0 at the 120–170 nm wavelength region. This function is in fact a result of our averaging the Table 2 function and, as can be readily verified, differs from it at all points by no more than 0.02. Figure 9 presents an efficiency curve (thin solid curve) calculated by use of these approximate values of the MgF_2 absorption index; all other parameters of model 3 remain intact. A comparison of the curve efficiencies (Fig. 9) based on scaled (thin solid curve) and exactly calculated (thick solid curve) values of absorption shows that the efficiency changes at the wavelengths where the RI imaginary values scale only slightly are indeed appreciable. This comparison once again stresses the need of a detailed numerical efficiency modeling to obtain accurate values of the unknown RIs; linear extrapolation or standard interpolations of known optical constants may induce significant errors into the calculated efficiency values.[9]

All calculations were performed using the PCGrate-S(X) v.6.1 software[7]; an accuracy parameter of 200–300 discretization points per each boundary was used. The total error derived from the energy balance does not exceed 1×10^{-4} at all points. Calculation time is $\sim$30 s for one data point in a general polarization state. Calculation was performed with an IBM ThinkPad portable workstation with an Intel Pentium M 1700 MHz processor, 1 Mbyte cache, 400 MHz bus clock, and 512 Mbytes RAM; the operating system used was Microsoft Windows XP Pro.

5. SUMMARY AND CONCLUSION

In conclusion, we sum up the results obtained and their possible application.

The exact MIM method, which is designed to solve problems of diffraction from multilayer gratings with arbitrary boundary shapes and layer thicknesses, including nonconformal layers and boundaries with real (e.g., AFM-measured) profiles, is a basis for the multilayer solver PCGrate-S(X)[7] used for the purpose of this work.

The FAUST scatterometer[23] has been used to measure the efficiency at the VUV–NUV range under various angles of incidence on a series of high-spatial-frequency gratings fabricated for the COS HST project, in particular the G185M subwavelength multilayer gratings.

Resonance anomalies and efficiency behavior as a function of the layer parameters (geometry and RI) and polarization of incident light have been investigated for the metal-coated grating overcoated with a nonconformal dielectric layer with real boundaries. The measured and modeled efficiencies of the highly resonant G185M grating with AFM-measured boundaries were found to agree within 9.6% of absolute efficiency in the extended wavelength range.

The tabulated MgF_2 RIs[5,26] are found to differ strongly from their actual values derived from the G185M grating study. Numerical efficiency modeling revealed that at wavelengths of 160 nm and below, the MgF_2 thin-film coating applied exhibits a noticeable absorption, a point also substantiated by known experimental data on optical constants.[6,27] We propose and describe in detail a method to obtain factual RIs based on comparing experimental efficiencies data with calculated values from MIM-based modeling using precise AFM-measured groove profile for the particular example of the G185M grating. The foregoing approach to derive the optical constants from grating efficiency is similar to the methods employed customarily for RI data deduction out of the reflectance and/or transmittance measurements of bulk and thin-films materials.[5] It is, however, independent and may turn out to be much more accurate due to the resonant nature of grating diffraction, especially near anomalous reflection or for the materials showing significant absorption at difficult to measure wave bands, for example, at EUV–VUV wavelengths.[24]

APPENDIX A: ENERGY BALANCE EQUATION FOR A MULTILAYER GRATING

Let d be the grating period, k_0 the wave vector of the incident wave in medium 0, and θ the angle of incidence. We denote as usual [see, e.g., Ref. 20, Eq. (1.42)]

$$\alpha_m = k_0 \cos\theta + 2\pi m/d, \quad m = 0, \pm 1, \pm 2, \ldots,$$

$$\beta_m^{(j)} = (k_j^2 - \alpha_m^2)^{1/2}, \tag{A1}$$

where $k_j = k_0(\nu_j/\nu_0)$ is the wavenumber in medium j and the square-root branch is such that $\mathrm{Re}(\sqrt{\ }) \geqslant 0$ and $\mathrm{Im}(\sqrt{\ }) \geqslant 0$. Note that $\beta_0^{(0)} = k_0 \sin\theta$. The reflected field in the far zone above the grating is a finite sum of propagating plane waves: for (x,y) in Λ_0,

$$u_{\mathrm{refl}}(x,y) = \sum_{|\alpha_m|<k_0} c_m^+ \exp(i\alpha_m x + i\beta_m^{(0)} y) + \text{evanescent waves} \tag{A2}$$

The reflection coefficient is defined as

$$R = \sum_{|\alpha_m|<k_0} |c_m^+|^2 \frac{\beta_m^{(0)}}{\beta_0^{(0)}}. \tag{A3}$$

If the lower medium is a lossless dielectric [$\mathrm{Im}(k_N)=0$ (case of transmission grating)], then we define the coefficients of the transmitted field for (x,y) in Λ_N:

$$u_{\mathrm{transm}}(x,y) = \sum_{|\alpha_m|<k_N} c_m^- \exp(i\alpha_m x - i\beta_m^{(N)} y) + \text{evanescent waves}, \tag{A4}$$

and the transmission coefficient

$$T = \left(\frac{\kappa_N}{\kappa_0}\right)^2 \sum_{|\alpha_m|<k_N} |c_m^-|^2 \frac{\beta_m^{(N)}}{\beta_0^{(0)}}. \tag{A5}$$

The polarization-dependent coefficients κ are defined as

$$\kappa_j = \begin{cases} 1 & \text{for TE polarization} \\ (\nu_j/\nu_{j+1})^2 = \varepsilon_j/\varepsilon_{j+1} & \text{for TM polarization} \end{cases}. \tag{A6}$$

In the case of a lossy medium Λ_N, as well as for a perfectly reflecting lower boundary, we set $T=0$.

If the grating is lossless, $\mathrm{Im}(k_j)=0$, $j=1,\ldots,N$, then conservation of energy is expressed by the standard energy criterion

$$R + T = 1. \tag{A7}$$

In the general case, the difference

$$A = 1 - (R + T) \geqslant 0 \tag{A8}$$

is called the absorption coefficient in the given diffraction problem. In addition to being physically meaningful, expression (A8) is useful as one of the accuracy tests for the computational code. The energy criterion in the lossless case says $A=0$. In the lossy case, one needs an independently calculated quantity to compare with A. For such a quantity, we use the absorption integral defined as the sum

$$I_A = \frac{1}{\beta_0^{(0)} d}\left[\mathrm{Im}\int_{\Gamma_0} u_0^{+}(v_0^{+})^{*}\mathrm{d}s - \left(\frac{\kappa_N}{\kappa_0}\right)^2 \mathrm{Im}\int_{\Gamma_{N-1}} u_{N-1}^{-}(v_{N-1}^{-})^{*}\mathrm{d}s \right]. \qquad \text{(A9)}$$

Here z^* means the complex conjugate of z. The functions u_0^+, u_{N-1}^- are the boundary values of the field on the outward faces of the grating and v_0^+, $(-v_{N-1}^-)$ are the boundary values of the outward normal derivatives (with respect to the slab). The second summand $\int_{\Gamma N-1}$ is not present if the lower layer is lossy or absent. The discrepancy $A-I_A$ is a measure of the numerical energy error.

ACKNOWLEDGMENTS

Helpful discussions with R. Keski-Kuha of NASA/GSFC and S. L. Zheleznyak of Newport's Richardson Gratings are greatly appreciated. The thorough work of the reviewers has led to a significant improvement of the exposition. Leonid I. Goray can be reached by e-mail at lig@pcgrate.com.

REFERENCES

1. J. C. Green, "Cosmic Origins Spectrograph," in *UV, Optical, and IR Space Telescopes and Instruments*, J. B. Breckinridge and P. Jakobsen, eds., Proc. SPIE **4013**, 352–359 (2000).
2. I. G. Kuznetsov, E. Wilkinson, D. A. Content, R. A. Boucarut, and T. J. Madison, "Grating efficiencies comparison study: calculations versus metrology for various types of high groove density gratings at VUV-UV wavelengths," in *Optical Modeling and Performance Predictions*, M. A. Kahan, ed., Proc. SPIE **5178**, 267–277 (2004).
3. R. Grange, V. Dauer, M. Saisse, M. Nevière, J. Flamand, and F. Bonnemason, "6000-g/mm holographic flight gratings for the high resolution Far Ultraviolet Spectroscopic Explorer: efficiency, resolution and stray light measurements," in *Theory and Practice of Surface-Relief Diffraction Gratings: Synchrotron and Other Applications*, W. R. McKinney and C. A. Palmer, eds., Proc. SPIE **3450**, 103–112 (1998).
4. V. Dauer, "Optical constants of lithium fluoride thin films in the far ultraviolet," J. Opt. Soc. Am. B **17**, 300–303 (2000).
5. E. Palik, ed., *Handbook of Optical Constant of Solids* (Academic, 1991), Vol. 2.
6. J. Larruquert and R. Keski-Kuha, "Far ultraviolet optical properties of $\mathrm{MgF_2}$ films deposited by ion-beam sputtering and their application as protective coatings for Al," Opt. Commun. **215**, 93–99 (2003).
7. See website at www.pcgrate.com.
8. D. A. Content, P. Arsenovic, I. G. Kuznetsov, and T. Hadjimichael, "Grating groove metrology and efficiency predictions from the soft x-ray to the far infrared," in *Optical Spectroscopic Techniques and Instrumentation for Atmospheric and Space Research IV*, A. M. Larar and M. G. Mlynczak, eds., Proc. SPIE **4485**, 405–416 (2001).
9. L. I. Goray and S. Yu. Sadov, "Numerical modeling of coated gratings in sensitive cases," in *Diffractive Optics and Micro-Optics*, R. Magnusson, ed., Vol. 75 of OSA Trends in Optics and Photonics Series (Optical Society of America, 2002), pp. 365–379.
10. D. Maystre, "A new general integral theory for dielectric coated gratings," J. Opt. Soc. Am. **68**, 490–495 (1978).
11. A. Pomp, "The integral method for coated gratings: computational cost," J. Mod. Opt. **38**, 109–120 (1991).
12. B. Kleemann, A. Mitreiter, and F. Wyrowski, "Integral equation method with parametrization of grating profile: theory and experiments," J. Mod. Opt. **43**, 1323–1349 (1996).
13. J. T. Beale and M.-C. Lai, "A method for computing nearly singular integrals," SIAM (Soc. Ind. Appl. Math.) J. Numer. Anal. **38**, 1902–1925 (2001).
14. K. E. Atkinson, *The Numerical Solution of Integral Equations of the Second Kind* (Cambridge U. Press, 1997).
15. G. Elschner and I. Graham, "An optimal order collocation method for first kind boundary integral equations on polygons," Numer. Math. **70**, 1–31 (1995).
16. R. Kress, "A Nyström method for boundary integral equations in domains with corners," Numer. Math. **58**, 145–161 (1990).
17. P. Laubin, "High order convergence for collocation of second kind boundary integral equations on polygons," Numer. Math. **79**, 107–140 (1998).
18. R. Kress, I. Sloan, and F. Stenger, "A sinc quadrature method for the double layer integral equation in planar domain with corners," J. Integral Equ. Appl. **10**, 291–317 (1998).
19. C. M. Linton, "The Green's function for two-dimensional Helmholtz equation in periodic domains," J. Eng. Math. **33**, 377–402 (1998).
20. R. Petit, ed., *Electromagnetic Theory of Gratings* (Springer, 1980).
21. A. Aho, J. Hopcroft, and J. Ullman, *The Design and Analysis of Computer Algorithms* (Addison-Wesley, 1976).
22. D. Knuth, *The Art of Computer Programming* (Addison-Wesley, 1998), Vol. 2.
23. I. G. Kuznetsov, D. A. Content, R. A. Boucarut, and T. J. Madison, "Design, performance and reliability of a high angular resolution, wide angular range, large aperture fully automated UV scatterometer," in *Optical Spectroscopic Techniques, Remote Sensing, and Instrumentation for Atmospheric and Space Research IV*, A. M. Larar and M. G. Mlynczak, eds., Proc. SPIE **4485**, 417–428 (2001).
24. J. F. Seely, L. I. Goray, D. L. Windt, B. Kjornrattanawanich, Yu. A. Uspenskii, and A. V. Vinogradov, "Extreme ultraviolet optical constants for the design and fabrication of multilayer gratings," in *Optical Constants of Materials for UV to X-Ray Wavelengths*, R. Soufli and J. F. Seely, eds., Proc. SPIE 5538, 43–52 (2004).
25. E. G. Loewen and E. Popov, *Diffraction Gratings and Applications* (Marcel-Dekker, 1997).
26. *American Institute of Physics Handbook* (McGraw-Hill, 1972).
27. R. Keski-Kuha, NASA GSFC, Code 551, Greenbelt, Maryland 20771 (personal communication 2005).
28. E. Spiller, *Soft X-ray Optics* (SPIE Press, 1994).
29. L. I. Goray, "Modified integral method and real electromagnetic properties of echelles," in *Diffractive and Holographic Technologies for Integrated Photonic Systems*, R. I. Sutherland, D. W. Prather, and I. Cindrich, eds., Proc. SPIE **4291**, 13–24 (2001).